Chinese Chemical Letters 35 (2024) 108974

Contents lists available at ScienceDirect

Chinese Chemical Letters

journal homepage: www.elsevier.com/locate/cclet

Aza-BODIPY dye with unexpected bromination and high singlet oxygen quantum yield for photoacoustic imaging-guided synergetic photodynamic/photothermal therapy

Leichen Wang[a], Anqing Mei[a], Na Li[a], Xiaohong Ruan[a], Xu Sun[a], Yu Cai[c], Jinjun Shao[a,*], Xiaochen Dong[a,b,*]

[a] Key Laboratory of Flexible Electronics (KLOFE) & Institute of Advanced Materials (IAM), Nanjing Tech University (NanjingTech), Nanjing 211800, China
[b] School of Chemistry & Materials Science, Jiangsu Normal University, Xuzhou 221116, China
[c] Center for Rehabilitation Medicine, Rehabilitation & Sports Medicine Research Institute of Zhejiang Province, Department of Rehabilitation Medicine, Zhejiang Provincial People's Hospital (Affiliated People's Hospital, Hangzhou Medical College), Hangzhou 310014, China

ARTICLE INFO

Article history:
Received 29 June 2023
Revised 23 August 2023
Accepted 24 August 2023
Available online 26 August 2023

Keywords:
Unexpected bromination
Aza-BODIPY
Photodynamic therapy
Photothermal therapy
Synergetic therapy

ABSTRACT

Introducing heavy halogen atoms into organic small molecules is a practical strategy for efficient singlet oxygen ($^1O_2$) generation. Generally, bromine or iodine atoms are introduced on the aza-boron-dipyrromethene (aza-BODIPY) core, rather than on the periphery aryl rings for efficient $^1O_2$ generation. Herein, an aza-BODIPY dye NBDPBr with unexpected bromination on the periphery aryl rings was synthesized for photoacoustic (PA) imaging-guided synergistic photothermal therapy (PTT) and photodynamic therapy (PDT) in tumor cells. Owing to unexcepted bromination at the periphery aryl rings, NBDPBr demonstrated an outstanding singlet oxygen quantum yield (Φ_Δ) of 66% which was superior to similar brominated photosensitizers previously reported. After encapsulation with amphiphilic polymer F-127, hydrophilic NBDPBr nanoparticles (NPs) were fabricated and exhibited an excellent photothermal conversion efficiency (η) of 43.0% under 660 nm photoirradiation. *In vivo* PA imaging results demonstrated that NBDPBr NPs could specifically accumulate at tumor sites and realized the maximum tumor retention at 7 h post-injection. All the *in vitro* and *in vivo* results indicated the significant potence of NBDPBr with unexpected bis-bromination for PA imaging-guided synergetic PDT/PTT.

Cancer, one of the most deadly diseases around the world, has promoted the progress of cancer phototheranostic at the same time assisted by its high morbidity and mortality [1]. Phototheranostic, including photo-diagnosis and phototherapy, as an emerging mode has attracted wide attention from researchers due to its characteristics of low toxicity, non-drug resistance, non-invasiveness and high targeting [2,3].

Although many phototheranostic agents can conquer the field of imaging-guided tumor photodynamic therapy (PDT) or photothermal therapy (PTT) [4,5]. However, single-mode phototherapy is challenging to achieve the purpose of tumor elimination [6]. On the one hand, the heat of PTT is difficult to ablate the tumor completely, and the residual cancer cells with overexpressed heat shock proteins will acquire resistance to heat stress, which results in limited therapeutic effect [7,8]. On the other hand, PDT is highly dependent on tissue oxygen, which results in limited therapeutic efficacy in the hypoxic tumor microenvironment for solid tumors [9–11]. Since PTT can enhance blood perfusion to relieve hypoxemia, and PDT can produce reactive oxygen species (ROS) to restrain heat shock proteins, combining PTT and PDT as synergistic therapy will be a practical strategy to improve the therapeutic effect [12,13].

Till now, many organic small molecule dyes have been exploited for tumor phototheranostics, including cyanine, porphyrin, phthalocyanine, diketopyrrolopyrrole (DPP), dipyrromethene boron difluoride (BODIPY)/aza-BODIPY, boron difluoride formazan (BDF), and benzothiadiazole derivatives [14–21]. Among them, aza-BODIPY-derived organic dyes have presented tunable molecular structures and outstanding photophysical properties of intensive near-infrared (NIR) absorption, high molar extinction coefficient (ε), and excellent photostability, which have been widely employed for application in tumor phototheranostics [22–25].

During the past two decades, many aza-BODIPY-based photosensitizers have been exploited with heavy atoms, such as Br or

* Corresponding authors.
E-mail addresses: iamjjshao@njtech.edu.cn (J. Shao), iamxcdong@njtech.edu.cn (X. Dong).

https://doi.org/10.1016/j.cclet.2023.108974
1001-8417/

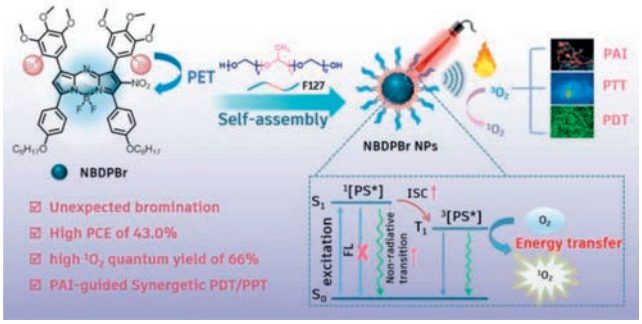

Scheme 1. Illustration for the preparation of NBDPBr NPs and the phototheranostic application.

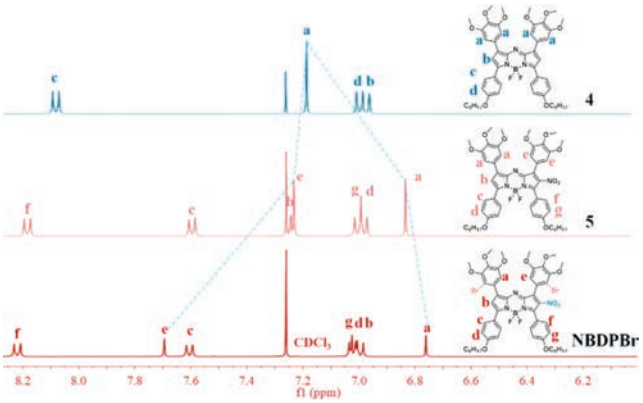

Fig. 1. Partial ^{1}H NMR spectra of **4**, **5**, and NBDPBr in $CDCl_3$.

I atoms, to enhance intersystem crossing (ISC) and facilitate spin-orbit coupling for efficient $^1O_2$ generation [26]. However, the halogenated sites showed a significant effect on $^1O_2$ production. Generally, aza-BODIPYs with heavy atoms on the central core give rise to higher $^1O_2$ generation than halogenation at the periphery aryl rings [27]. This phenomenon would be attributed to the different modulated degree of spin-orbit coupling. On the one hand, positioning of heavy atoms on the periphery aryl rings would exhibit ordinary singlet-oxygen generation due to an external heavy-atom effect [28,29]. While directly introducing heavy atoms onto the photosensitizer core would provide efficient singlet-oxygen generation by taking advantage of the internal heavy-atom effect [27,30]. Meanwhile, as described by the Jablonski diagram, there is a competitive relationship between radiative decay, non-radiative decay, and intersystem crossing; therefore, ideal small molecule dyes could be reasonably designed with the on-demand tuning of the excited states for high-performance phototheranostics [31,32].

Herein, a novel aza-BODIPY dye NBDPBr with unexpected bromination on the periphery aryl rings was constructed for PA imaging-guided synergistic PTT and PDT in tumor cells (Scheme 1). Surprisingly, the unexpected bis-bromination at the periphery phenyl rings of aza-BODIPY endowed NBDPBr with a high $^1O_2$ quantum yield (Φ_Δ) of 66%. Through self-assembly, NBDPBr was encapsulated by Pluronic® F-127 to fabricate NBDPBr NPs with good biocompatibility and water-solubility, which could achieve tumor accumulation through enhanced permeability and retention (EPR) effect. Moreover, owing to the photoinduced electron transfer (PET) effect of the nitro group, the fluorescence of NBDPBr was significantly quenched, thus enhancing the non-radiative transition to improve the photothermal effect with the photothermal conversion efficiency of 43.0% upon 660 nm photoirradiation. Meanwhile, the remarkable photothermal effect enables NBDPBr NPs a good photoacoustic (PA) response. The *in vitro* and *in vivo* studies demonstrated the great potential of the bis-brominated NBDPBr for PA imaging-guided synergetic PDT/PTT.

As shown in Scheme S1 (Supporting information), aza-BODIPY dye 4 was readily obtained through multi-step synthesis, which started from the preparation of chalcone **1** through aldol condensation [33]. Subsequently, compound **2** was synthesized through a Michael addition reaction between chalcone **1** and nitromethane in a yield of 64%. Refluxing of **2** in *n*-butanol in the presence of NH_4OAc afforded **3**, which was further reacted with boron trifluoride to give **4**. Then, the reaction of **4** in HNO_3 solution at 0 °C resulted in nitrated **5** in 63% yield. Considering the efficient $^1O_2$ generation by directly introducing halogen atoms on the aza-BODIPY core, *N*-bromosuccinimide (NBS) was applied as the bromination agent [27]. Unexpectedly, the bromine atoms were connected to the periphery aryl rings of aza-BODIPY to afford bis-brominated NBDPBr, which was verified by ^{1}H nuclear magnetic resonance (NMR) and ^{1}H-^{1}H correlated spectroscopy (COSY) NMR. In Fig. 1, the partial ^{1}H NMR spectra of NBDPBr and **5** showed the chemical shift changes of proton a and proton e, indicating the successful introduction of bromine atoms. As shown in the ^{1}H-^{1}H COSY NMR of NBDPBr (Fig. S1 in Supporting information), interactions between protons c and d, protons f and g, could be clearly observed. Nonetheless, protons a, b, and e did not show any interactions, which was consistent with their appearance of singlet peaks, further confirming the chemical structure of NBDPBr. All intermediates and the bis-brominated NBDPBr were characterized by ^{1}H NMR, ^{13}C NMR, liquid chromatography-mass spectrometry (LC-MS), and matrix-assisted laser desorption/ionization-time of flight mass spectrometry (MALDI-TOF MS) (Supporting information).

The bromine atoms in the bis-brominated NBDPBr are anticipated to facilitate spin-orbit coupling and enhance the ISC process to strengthen the $^1O_2$ generation [34,35]. Therefore, taking 1,3-diphenylisobenzofuran (DPBF) as the probe, the $^1O_2$ generation performance of NBDPBr was studied in dichloromethane (DCM) by monitoring the absorption decay of DPBF at 418 nm under 660 nm photoirradiation (Fig. 2a). And a fast absorbance decrease of DPBF was observed, indicating a sufficient $^1O_2$ production of NBDPBr. Employing methylene blue (MB, $\Phi_\Delta = 57\%$ in DCM) as the standard [36], bis-brominated NBDPBr exhibited a high $^1O_2$ quantum yield (Φ_Δ) of 66% (Fig. 2b and Fig. S2a in Supporting information), which was superior to a series of similar brominated photosensitizers that had been reported (Fig. 2c and Table S2 in Supporting information) [37–40], indicating the outstanding $^1O_2$ generation capability of NBDPBr for further PDT application.

To improve the water solubility of NBDPBr for further phototheranostics application, amphipathic copolymer Pluronic® F-127 was employed to co-assemble with NBDPBr for the fabrication of NBDPBr NPs. The scanning electron microscope (SEM) image indicated a spherical morphology of NBDPBr NPs with a diameter of around 70 nm (Fig. 2d). And the dynamic light scattering (DLS) result demonstrated that the hydrodynamic size of NBDPBr NPs was 84 nm with a polydispersity index (PDI) of 0.168, which was suitable for passive targeting through the EPR effect. In addition, there was no sedimentation or aggregation of NBDPBr NPs in the aqueous solution within one week and the hydrodynamic size of NBDPBr NPs did not show any noticeable change during one week, suggesting excellent stability of NBDPBr NPs (Fig. S3 in Supporting information).

To study the photophysical properties, the absorption and fluorescence spectra of this bis-brominated NBDPBr dye in organic solvents and NBDPBr NPs in water were recorded (Fig. 2e and Fig. S4 in Supporting information). And the photophysical properties of compounds **4**, **5**, NBDPBr, and NBDPBr NPs were summarized in Table S1 (Supporting information). The absorption peak of NBDPBr in DCM and NBDPBr NPs in water appeared at 642 nm,

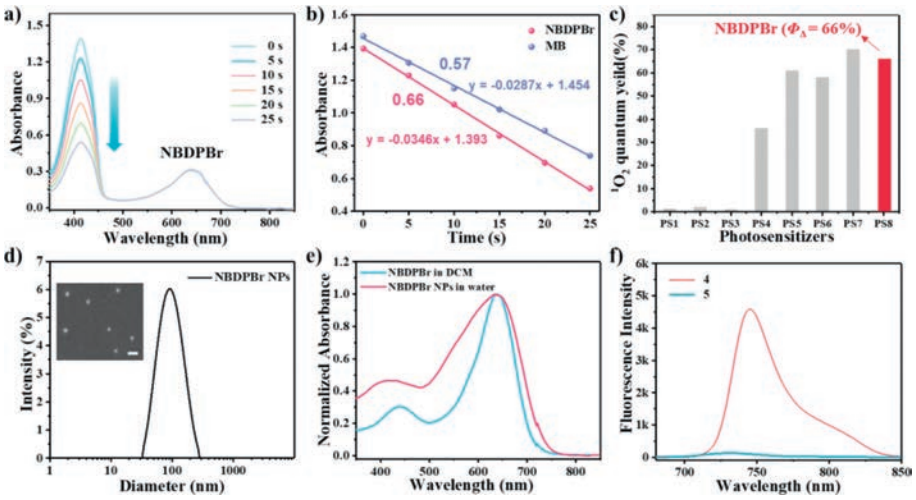

Fig. 2. (a) Absorbance decay of DPBF in DCM with the presence of NBDPBr upon 660 nm photoirradiation (10 mW/cm^2). (b) The fitted linear relationship between the absorbance of DPBF at 418 nm and irradiation time in the presence of NBDPBr or MB. (c) $^1O_2$ quantum yield comparison of NBDPBr and reported photosensitizers with bromination at the periphery aryl rings (Table S2) [37–40]. (d) SEM image and DLS size distribution of NBDPBr NPs. Scale bar: 200 nm. (e) Normalized absorbance of NBDPBr and NBDPBr NPs. f) Fluorescence spectra of **4** and **5** (10 μmol/L, in DCM), λ_{ex} = 650 nm.

Table 1
Electrochemical data and energy levels of NBDPBr.

Cpd.	HOMO/eV		LUMO/eV		E_g^{cv}/eV	E_g^{opt}/eV[c]
	CV[a]	Calc[b]	CV[a]	Calc[b]		
NBDPBr	−5.61	−5.40	−4.10	−3.30	1.51	1.75

[a] From the CV results, HOMO = −(4.80 + E_{ox}^{onset}), and LUMO = −(4.80 + E_{red}^{onset}).
[b] From the calculated results.
[c] E_g^{opt} was obtained from the lowest-energy absorption edge in DCM.

and their extinction coefficients were calculated to be 3.62 × 10^4 L mol^{-1} cm^{-1} and 21.0 L g^{-1} cm^{-1} at 660 nm, respectively (Fig. S5 in Supporting information). NBDPBr dye showed a relatively weak fluorescence covering from 650 nm to 850 nm with peaks at around 715 nm in organic solvents with different polarities. While NBDPBr NPs showed almost no fluorescence, owing to the aggregation-caused quenching effect [41]. In addition, the fluorescence spectra of **4** and **5** in DCM were recorded for comparison; it was apparent that nitrated **5** presented a strong fluorescence quenching phenomenon in contrast to **4**, which was attributed to the PET effect between the electron-deficient nitro group and aza-BODIPY dye [42–44]. And usually, the PET effect could weaken the radiative transition to enhance the non-radiative transition for enhanced PTT (Fig. 2f) [45].

The electrochemical properties of NBDPBr were investigated by cyclic voltammetry (CV) and differential pulse voltammetry (DPV) measurements in anhydrous DCM with Fc/Fc$^+$ as reference (Fig. S6 in Supporting information). The highest occupied molecular orbital (HOMO), lowest unoccupied molecular orbital (LUMO) energy levels, and energy gaps are summarized in Table 1. Two *quasi*-reversible reduction waves were found for NBDPBr, with the reduction potential onset (E_{red}^{onset}) of −0.70 V, and half-wave potential $E_{red}^{1/2}$ of −1.49 and −0.72 V (Figs. S6c and d). Meanwhile, NBDPBr displayed two *quasi*-reversible oxidation waves, exhibiting the onset of oxidation potential (E_{ox}^{onset}) at 0.81 V with the half-wave potential $E_{ox}^{1/2}$ of 0.91 and 1.09 V. Therefore, the HOMO/LUMO energy levels derived from E_{ox}^{onset} and E_{red}^{onset} were −5.61 and −4.10 eV, respectively [46]. Therefore, the energy gap E_g^{cv} was determined to be 1.51 eV, which was in good agreement with the optical energy gap (E_g^{opt}) of 1.75 eV Then, the time-dependent density functional theory (TD-DFT) at the B3LYP/6-31G(d,p) levels

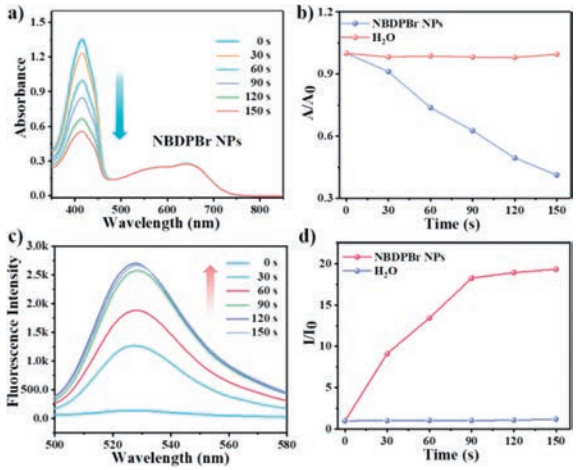

Fig. 3. (a) Absorbance decay of DPBF and (c) Fluorescence increase of SOSG in the presence of NBDPBr NPs under 660 nm irradiation (50 mW/cm^2). (b) Absorbance change of DPBF at 418 nm and (d) Fluorescence increase of SOSG at 525 nm along with exposure time.

was used to theoretically investigate the electron density distribution and the molecular architecture fundamentals for this bis-brominated dye NBDPBr. The theoretical calculations demonstrated that the calculated HOMO/LUMO energy levels and energy gap were −5.40/−3.30 and 2.10 eV of NBDPBr, respectively (Fig. S7 in Supporting information).

Moreover, to further characterize the $^1O_2$ generation performance of NBDPBr NPs, DPBF and singlet oxygen sensor green (SOSG) were chosen as the $^1O_2$ probe to detect the yield of $^1O_2$ by quantifying the fluorescence enhancement of SOSG at 525 nm, and the absorbance decay of DPBF at 418 nm. Upon 660 nm photoirradiation (50 mW/cm^2) for 150 s, the absorbance change for the mixed solution of DPBF and NBDPBr NPs and the fluorescence increase for the mixed solution of SOSG and NBDPBr NPs were recorded. As shown in Fig. 3, a fast absorbance decrease of DPBF at 418 nm, and a rapid increase of the fluorescence intensity of SOSG solution at 525 nm could be observed, indicating a plentiful $^1O_2$ production of NBDPBr NPs. As demonstrated that NBDPBr NPs could be an excellent therapeutic nanoagent for PDT.

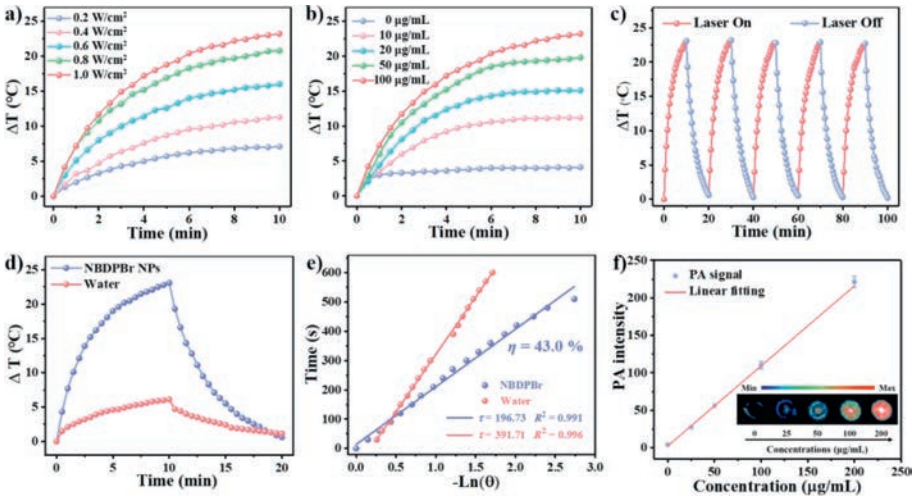

Fig. 4. (a) Photothermal profiles of NBDPBr NPs under 660 nm irradiation with exposure to different power intensities. (b) Photothermal profiles of NBDPBr NPs at different concentrations under 660 nm irradiation. (c) Photothermal stability test of NBDPBr NPs upon 660 nm photoirradiation (1.0 W/cm^2). (d) Photothermal curves of NBDPBr NPs and water under 660 nm irradiation (1.0 W/cm^2) for 10 min followed by cooling to room temperature. (e) Linear correlation of the cooling times against negative natural logarithm of driving force temperatures. (f) *In vitro* PA images and fitted linear relationship of PA intensities against the concentrations of NBDPBr NPs.

The intensive absorption with high extinction coefficient motivated us to assess the photothermal behavior of NBDPBr NPs. The photothermal conversion of NBDPBr NPs was investigated with 660 nm photoirradiation. As exhibited in Fig. 4a, the photothermal effect exhibited a positive correlation with both the laser power density and the photoirradiation time, revealing a controllable photothermal behavior. Meanwhile, the temperature increment profiles of NBDPBr NPs showed a prominent concentration dependence, with the maximum temperature increase of 23.2 °C within 10 min irradiation by 660 nm laser (1.0 W/cm^2); whereas the water exhibited a negligible temperature enhancement under the same condition (Figs. 4b and d). On the basis of the temperature change in the cooling stage, the photothermal conversion efficiency (η) of NBDPBr NPs was calculated as 43.0%, presenting its potential for tumor PTT (Fig. 4e) [47,48]. Additionally, the temperature change showed almost no decrease of NBDPBr NPs after five cycles of photoirradiation-heating and natural cooling, suggesting its outstanding photothermal stability (Fig. 4c). Meanwhile, using the clinically approved NIR dye indocyanine green (ICG) for comparison, the photostability of NBDPBr NPs was studied through 660 nm photoirradiation (Fig. S8 in Supporting information). Within 8 min photoirradiation, a fast absorbance decrease of ICG was observed; nevertheless, the absorbance of NBDPBr NPs exhibited almost no change, demonstrating its outstanding photostability. The excellent photothermal stability and photostability of NBDPBr NPs provided a precondition for phototheranostic.

As is known to all, photothermal nanoagent convert absorbed photon energy into heat upon photoirradiation, and the ultrasonic waves are then generated through thermoelastic collisions and pressure transients in the tissues. Finally, PA signals can be obtained [49,50]. And ultraviolet and visible (UV–vis) absorption and photothermal conversion of the photothermal nanoagent play a key role for PA brightness [51–53]. Therefore, owing to the outstanding photothermal effect of NBDPBr NPs, an obvious PA signal could be observed upon 660 nm excitation. And the PA intensities presented a steady enhancement along with the concentration of NBDPBr NPs from 0 to 200 μg/mL, exhibiting a representative linear relationship (R^2 = 0.998, Fig. 4f). The resulting data indicated the potential of NBDPBr NPs as PA contrast nanoagent for PA imaging-mediated tumor phototherapy.

To study the biocompatibility and phototoxicity of NBDPBr NPs, the viability of 4T1 tumor cells treated by NBDPBr NPs was examined *via* MTT (3-(4,5-dimethylthiazol2-yl)−2,5-diphenyltetrazolium bromide) assay. The dose-dependent cell toxicity of NBDPBr NPs under the condition of dark and photoirradiation was evaluated. As shown in Fig. 5a, NBDPBr NPs did not trigger discernible cytotoxicity to 4T1 cells in the dark, and more than 90% cell viability was observed even at a high concentration of 100 μg/mL, suggesting good biocompatibility of NBDPBr NPs. In contrast, upon 660 nm photoirradiation (0.8 W/cm^2, 5 min), the viability of 4T1 tumor cells significantly decreased along with increasing NBDPBr NPs concentration, indicating great phototoxicity of NBDPBr NPs. The results manifested that NBDPBr NPs with high photothermal conversion and good $^1O_2$ generation displayed excellent phototoxicity to tumor cells.

The photodynamic effect of NBDPBr NPs at the cellular level was further investigated, and the 2′,7′-dicholorofluoroescein diacetate (DCFH-DA) was applied as a fluorescent ROS probe indicator to monitor intracellular ROS generation in 4T1 tumor cells. After the reaction between DCFH-DA and intracellular ROS, 2′,7′-dichlorofluorescein (DCF) will be produced to show a green fluorescence under the excitation at 488 nm. Compared to the groups of phosphate-buffered saline (PBS), PBS+L, and NBDPBr NPs, only the group NBDPBr NPs+L displayed bright green fluorescence, indicating effective intracellular ROS generation under 660 nm illumination (Fig. 5c). As results confirmed the outstanding intracellular ROS generation for PDT mediated by NBDPBr NPs.

To further qualitatively verify the phototherapeutic efficacy of NBDPBr NPs, a live-dead cell staining experiment was carried out under 660 nm photoirradiation (0.8 W/cm^2) by staining the living cells with calcein AM (green) and tracking dead cells with propidium iodide dyes (red). As exhibited in Fig. 5b, intense red fluorescence was observed in the group of NBDPBr NPs+L, indicating that nearly all 4T1 cells were killed by NBDPBr NPs after 660 nm photoirradiation (0.8 W/cm^2, 8 min). Nonetheless, strong green fluorescence could be observed in the groups of PBS, PBS+L, and NBDPBr NPs, demonstrating good biocompatibility for NBDPBr NPs. As results showed good consistency with the MTT results, suggesting the excellent phototherapeutic efficacy of NBDPBr NPs.

With these promising *in vitro* studies, *in vivo* investigation of tumor PA imaging and photothermal imaging were carried out. All experimental animal procedures were performed with approval from the Institutional Animal Care and Use Committee of the Hospital of Zhejiang Province. Taking 4T1 tumor-xenografted mice as

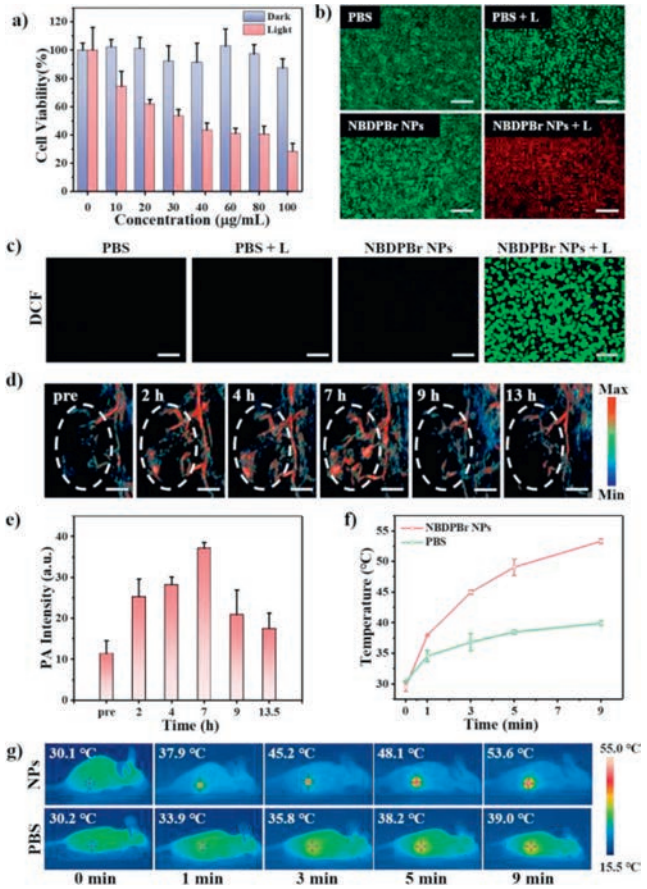

Fig. 5. (a) Viability of 4T1 tumor cells after treatment with NBDPBr NPs. (b) 4T1 cells staining by calcein-AM/propidium iodide (PI) with green fluorescence ($\lambda_{ex}/\lambda_{em}$ = 494/517 nm, live cells) or red fluorescence ($\lambda_{ex}/\lambda_{em}$ = 535/617 nm, dead cells). Scale bar: 200 μm. L: Laser. (c) Fluorescence images of 4T1 tumor cells after 4 h incubation, followed by staining with DCFH-DA. Green fluorescence represents DCF (λ_{ex} = 488 nm). Scale bar: 100 μm. (d) PA images, and (e) PA intensities at tumor sites at pre-injection and various time spots after administration of NBDPBr NPs. Scale bar: 2 mm. (f) Temperature-change curves of tumor tissues along with photoirradiation periods. (g) Photothermal imaging of mice bearing 4T1 tumor treated with NBDPBr NPs and PBS under photoirradiation.

the model, NBDPBr NPs in PBS were firstly tail-vein injected to study *in vivo* PA imaging performance, and PA images of the mice were captured at various time spots (Figs. 5d and e). The PA signals of the tumor tissues exhibited prominent time dependence, and the PA intensities came to the maxima at 7 h post-injection and then gradually decreased. Meanwhile, the relative PA signals of the tumor tissues at 7 h post-injection showed a 3.3-fold enhancement than that of the pre-injection, suggesting the effective tumor accumulation of NBDPBr NPs.

Owing to the excellent photothermal effect, NBDPBr NPs were anticipated to be a candidate for photothermal imaging. Therefore, *in vivo* photothermal imaging behaviors of NBDPBr NPs were studied through the mice bearing 4T1 tumor. After 7 h post-injection of NBDPBr NPs, the tumor temperature of the mice increased from 30.1 °C to 53.6 °C within 9 min under 660 nm photoirradiation (0.8 W/cm^2), which was high enough to cause tumor cell ablation (Figs. 5f and g). However, the tumor temperature of the mice treating with PBS only increased from 30.2 °C to 39.0 °C. All results demonstrated that NBDPBr NPs were suitable for *in vivo* photothermal imaging-guided phototherapy.

In summary, an aza-BODIPY dye NBDPBr with unexpected bromination on the periphery aryl rings was constructed for PAI-guided synergetic PTT and PDT. Through self-assembly, NBDPBr was encapsulated by Pluronic® F-127 to fabricate hydrophilic NBDPBr NPs. Through the photophysical investigations, bis-brominated NBDPBr demonstrated an outstanding singlet oxygen quantum yield (Φ_Δ) of 66%, and NBDPBr NPs showed a good photothermal conversion efficiency (η) of 43.0% with 660 nm photoirradiation. Additionally, *in vivo* PA imaging showed that NBDPBr NPs could efficiently accumulate at tumor sites, and the PA intensities reached the maxima at 7 h post-injection. The photothermal imaging results exhibited that the tumor temperature could increase to 53.6 °C under 660 nm photoirradiation. *In vitro* and *in vivo* experiments demonstrated outstanding biocompatibility, good PA imaging performance, and synergetic PDT/PTT efficacy of NBDPBr NPs. Furthermore, the unexpected bromination of NBDPBr is believed to be a practical way for the development of effective phototheranostic agents.

Declaration of competing interest

The authors declare that they have no known competing financial interests or personal relationships that could have appeared to influence the work reported in this paper.

Acknowledgments

The work was supported by NSF of Jiangsu Province (No. BK20200092). We are also grateful to the High-Performance Computing Center in Nanjing Tech University for supporting the computational resources.

Supplementary materials

Supplementary material associated with this article can be found, in the online version, at doi:10.1016/j.cclet.2023.108974.

References

[1] H. Sung, J. Ferlay, R. Siegel, et al., CA Cancer J. Clin. 71 (2021) 209–249.
[2] X. Li, J. Lovell, J. Yoon, X. Chen, Nat. Rev. Clin. Oncol. 17 (2020) 657–674.
[3] B. Vickerman, E. Zywot, T. Tarrant, D. Lawrence, Nat. Rev. Chem. 5 (2021) 816–834.
[4] P. Cheng, K. Pu, ACS Appl. Mater. Interfaces 12 (2020) 5286–5299.
[5] V. Nguyen, J. Ha, M. Cho, et al., Coord. Chem. Rev. 439 (2021) 213936.
[6] X. Wei, C. Zhang, S. He, et al., Angew. Chem. Int. Ed. 61 (2022) e202202966.
[7] F. Zeng, L. Tang, Q. Zhang, et al., Angew. Chem. Int. Ed. 61 (2022) e202112925.
[8] X. Song, Q. Chen, Z. Liu, Nano Res. 8 (2014) 340–354.
[9] D. Chen, C. Liang, X. Qu, et al., Biomaterials 292 (2023) 121944.
[10] T. Pham, V. Nguyen, Y. Choi, et al., Chem. Rev. 121 (2021) 13454–13619.
[11] H. Chen, J. Tian, W. He, Z. Guo, J. Am. Chem. Soc. 137 (2015) 1539–1547.
[12] Y. Liu, C. Xu, L. Teng, et al., Chem. Commun. 56 (2020) 1956–1959.
[13] X. Li, F. Fang, B. Sun, et al., Nanoscale Horiz. 6 (2021) 177–185.
[14] J. Mu, M. Xiao, Y. Shi, et al., Angew. Chem. Int. Ed. 61 (2022) e202114722.
[15] H. Li, H. Kim, F. Xu, et al., Chem. Soc. Rev. 51 (2022) 1795–1835.
[16] P. Lo, M. Rodriguez-Morgade, R. Pandey, et al., Chem. Soc. Rev. 49 (2020) 1041–1056.
[17] Z. Cheng, T. Zhang, W. Wang, et al., Chin. Chem. Lett. 32 (2021) 1580–1585.
[18] L. Li, Y. Chen, W. Chen, et al., Chin. Chem. Lett. 30 (2019) 1689–1703.
[19] Q. Ma, X. Sun, W. Wang, et al., Chin. Chem. Lett. 33 (2022) 1681–1692.
[20] J. Tian, B. Huang, M. Nawaz, W. Zhang, Coord. Chem. Rev. 420 (2020) 213410.
[21] H. Li, H. Dai, A. Mei, et al., Dyes Pigments 205 (2022) 110478.
[22] D. Chen, Y. Tang, J. Zhu, et al., Biomaterials 221 (2019) 119422.
[23] D. Chen, Z. Zhong, Q. Ma, et al., ACS Appl. Mater. Interfaces 12 (2020) 26914–26925.
[24] P. Chinna Ayya Swamy, G. Sivaraman, R. Priyanka, et al., Coord. Chem. Rev. 411 (2020) 213233.
[25] Y. Wang, D. Zhang, K. Xiong, et al., Chin. Chem. Lett. 33 (2022) 115–122.
[26] Z. Shi, X. Han, W. Hu, et al., Chem. Soc. Rev. 49 (2020) 7533–7567.
[27] A. Gorman, J. Killoran, C. O'Shea, et al., J. Am. Chem. Soc. 126 (2004) 10619–10631.
[28] A. Chandra, N. Turro, A. Lyons, P. Stone, J. Am. Chem. Soc. 100 (1978) 4964–4968.
[29] D. Gao, B. Zhang, Y. Liu, et al., Theranostics 9 (2019) 5315–5331.
[30] D. Chen, Q. Tang, J. Zou, et al., Adv. Healthc. Mater. 7 (2018) e1701272.
[31] Z. Lei, F. Zhang, Angew. Chem. Int. Ed. 60 (2021) 16294–16308.
[32] G. Feng, G. Zhang, D. Ding, Chem. Soc. Rev. 49 (2020) 8179–8234.
[33] H. Cheng, X. Cao, S. Zhang, et al., Adv. Mater. 35 (2023) e2207546.
[34] Z. Xiong, Z. Wang, L. Liu, et al., Adv. Opt. Mater. 9 (2021) 2101228.

[35] Z. Wang, L. Huang, Y. Yan, et al., Angew. Chem. Int. Ed. 59 (2020) 16114–16121.
[36] T. Xiong, M. Li, X. Zhao, et al., Sens. Actuator. B: Chem. 304 (2020) 127310.
[37] M. Obłoza, Ł. Łapok, T. Pędziński, M. Nowakowska, Asian J. Org. Chem. 8 (2019) 1879–1892.
[38] N. Adarsh, M. Shanmugasundaram, R. Avirah, D. Ramaiah, Chemistry 18 (2012) 12655–12662.
[39] Y. Gawale, N. Adarsh, S. Kalva, et al., Chemistry 23 (2017) 6570–6578.
[40] N. Adarsh, R. Avirah, D. Ramaiah, Org. Lett. 12 (2010) 5720–5723.
[41] D. Ding, K. Li, B. Liu, B. Tang, Acc. Chem. Res. 46 (2013) 2441–2453.
[42] S. Li, F. Huo, C. Yin, Chem. Commun. 58 (2022) 12642–12652.
[43] J. Wu, J. Zhai, B. Wang, et al., Dyes Pigments 202 (2022) 110220.
[44] X. Meng, J. Zhang, Z. Sun, et al., Theranostics 8 (2018) 6025–6034.
[45] Y. Lyu, Y. Fang, Q. Miao, et al., ACS Nano 10 (2016) 4472–4481.
[46] Z. Wang, Q. Ma, X. Huang, et al., Chin. Chem. Lett. 33 (2022) 271–275.
[47] X. Wang, Z. Jiang, Z. Liang, et al., Sci. Adv. 8 (2022) eadd5660.
[48] C. Ye, S. Zhang, D. Zhang, et al., Chin. Chem. Lett. 34 (2023) 108223.
[49] Q. Shen, L. Wang, X. Ruan, et al., Adv. Funct. Mater. 33 (2023) 2300023.
[50] T. Yan, M. Su, Z. Wang, J. Zhang, Small (2023) e2300539.
[51] Y. Lyu, J. Zeng, Y. Jiang, et al., ACS Nano 12 (2018) 1801–1810.
[52] X. Zhen, K. Pu, X. Jiang, Small 17 (2021) e2004723.
[53] Y. Lyu, J. Li, K. Pu, Small Methods 3 (2019) 1900553.